Nanostructures in a binary mixture confined in slit-like pores with walls decorated with tethered polymer brushes in the form of stripes: Dissipative particle dynamics study

Jaroslav M. Ilnytskyi,[1,a)] Taras Patsahan,[1] and Stefan Sokołowski[2]
[1]*Institute for Condensed Matter Physics of National Academy of Sciences of Ukraine, 1 Svientsitskii Str, 79011 Lviv, Ukraine*
[2]*Department for the Modelling of Physico-Chemical Processes, Maria Curie-Skłodowska University, 20031 Lublin, Poland*

(Received 14 February 2011; accepted 26 April 2011; published online 23 May 2011)

Using dissipative particle dynamics, we investigate the behavior of a binary mixture, exhibiting demixing in a bulk phase, confined in slit-like pores with walls modified by the stripes of tethered brush of chains. Our main interest is to determine possible morphologies that can be formed inside the pore, depending on the geometrical parameters characterizing the system (the size of the pore and the width of the stripes). In order to describe the observed morphologies we calculate several characteristics, as the density and local temperature profiles, the radii of gyration for the attached polymers, and the minimum polymer-polymer distances in the direction parallel and perpendicular to the pore walls. The summary of our findings is presented as a sketch of the diagram of morphologies.
 [doi:10.1063/1.3592562]

I. INTRODUCTION

Surfaces modified with tethered polymer brushes have received a considerable amount of attention over past decades. This is because tethering of polymers offers a convenient way to modify, in a controllable fashion, several physico-chemical properties of surfaces,[1–5] and because such materials find applications in many important technological fields, such as wetting, adhesion, colloid stabilization, and biocompatibility, etc. Moreover, chemically bonded polymers are used as stationary phases in chromatography.[6–8]

Theoretical studies of equilibrium properties of surfaces with tethered brushes, as well as such surfaces in contact with fluids, have been carried out employing different approaches, including scaling theories,[9–11] classical self-consistent field methods,[12–14] mean-field approaches,[15,16] density functional theory,[17–21] and computer simulations at both molecular,[20–32] and mesoscopic levels. The latter have been mainly based on the dissipative particle dynamics (DPD).[33–45] DPD is a mesoscopic simulation technique that uses beads which do not represent actual molecules but rather groups of molecules, or alternatively, they can be thought of as fluid packets.

One of the first DPD studies of polymer-coated surfaces was carried out by Gibson *et al.*,[34] who investigated the adsorption of colloidal particles on a surface modified with pinned polymers. The results were in a good agreement with the theoretical predictions, namely, they indicated that the adsorption of colloidal particles was smaller when the size of the polymer relative to the colloidal particle and density of the polymers increased. Moreover, the adsorption was reduced when the polymer was well solvated. Malfreyt and Tildesley[36] used DPD to simulate grafted polymer brushes in slit-like pores with chains tethered at two walls. The tethered chains were immersed in a good solvent. The obtained polymer density profiles showed a parabolic shape across the pore. The diffusion along the pore axis was significantly greater for the solvent particles in the middle of the slab than for those in the polymer region since the solvent molecules were trapped within the entangled polymer. Moreover, Goujon, Malfreyt, and Tildesley[37] extended DPD method to the grand canonical ensemble to study the compression of grafted polymer brushes in good solvent conditions.

Wijmans and Smit[38] applied DPD to simulate constant and oscillatory shear flow between two flat plates with tethered chains. Pastorino *et al.*[39] investigated a short-chain melt between two brush-covered surfaces in equilibrium and under shear. The polymers of both brush and melt were identical. They studied the interdigitation of the melt and the brush and also considered the orientation of bond vectors on different length scales, as well as radii of gyration, end-to-end vectors of free and grafted chains, and in the case of nonequilibrium simulations, the velocity profiles. In the second work[40] Pastorino *et al.* used the Gibbs criterion to localize the brush-melt interface and analyzed its equilibrium fluctuations in terms of a capillary wave Hamiltonian augmented by an elastic term that accounts for the deformability of the brush. However, one should stress that the simulation method used in Refs. 39 and 40 was different from standard DPD scheme. For example, Pastorino *et al.* assumed that the interactions between the polymer segments and polymer segments with surfaces were of the Lennard-Jones type, and they performed molecular dynamics simulations with DPD thermostat[46–48] to simulate at constant temperature and to account for hydrodynamic interactions due to the conservation of total momentum.

Li *et al.*[43] applied DPD to investigate the surface structures of tethered rod-coil polymers. When immersed in a selective solvent for the coil blocks, rod blocks tend to form

a)Electronic mail: iln@icmp.lviv.ua.

aggregates. Linear and Y-shaped polymers exhibited similar aggregative behavior, but comb-like brushes were found to possess more diverse aggregative manners compared to linear brushes. Surface structures with aggregates taking the forms of cones, cylinders, or layers of spheres were found. The behavior of grafted binary polymer brushes with compatible components in the cases of different chain lengths was investigated by Xue *et al.*[45] They observed layered structures parallel to the surface indicating "phase separation": short chains were suppressed in the layer adjacent to the surface, whereas longer chains were much stretched. By slightly changing the solvent selectivity to prefer the short chains, a reversion of the layered structure was found.

The emergence of several novel techniques in material science[49] has permitted the fabrication of solid substrates with stable, precisely characterized, surface structures on length scales ranging from microns to nanometres.[49] The potential importance of structured substrates is connected with a possibility in the manipulation of fluids at very short length scales. Recent advances in nanotechnology have also permitted development of methods for obtaining functional polymeric films on solid surfaces exhibiting quite complex topographic nanostructures.[50] Indeed, the fabrication of structured polymer layers on solids is one of the major challenges in micro- and nanotechnology.

The potential importance of systems involving structured brushes in the manipulation of fluids at very short length scales has spurred parallel theoretical and simulational studies. A prototypical case consists of a solvent in contact with a surface, or confined between two identical plane-parallel substrates, decorated with stripes of tethered chains that alternate periodically in one direction (say, X) and are infinite in the other transverse direction (Y). Theoretical studies of such systems involve Monte Carlo (for both lattice and off-lattice models) and molecular dynamics,[51] self-consistent field methods,[52] and DPD simulations.[41,43] These studies indicated that heterogeneity of tethered layers has a great impact on the structure of the confined fluid and thermodynamic and dynamic properties of the systems. In particular, Patra and Linse[41] used DPD to examine the limit at which small-scale nanopatterned polymer brushes demonstrate the behavior similar to homogeneously grafted brushes. They also proposed scaling relations for the brush height and brush width for different geometries of the system. Petrus *et al.*[43] considered the case of symmetric diblock copolymers confined between planar surfaces with and without nanopatterns. The nanopatterned surface was mimicked by alternating portions of the surface that interacted differently with the different beads constituting the diblock copolymers. They investigated the formation of diblock copolymer nanostructures confined between planar, nonmodified surfaces and observed both perpendicular and parallel lamellar phases with different numbers of lamellae. In the case of nanopatterned slits, they observed novel nanostructures and attempted to rationalize the diblock copolymer self-assembly on the basis of the behavior that was observed without nanopatterns.

In adsorption and in chromatographic experiments the fluid in contact with a modified surface is usually a multicomponent one. Therefore, it is of interest to investigate how the structure of the system involving a two-component solution is influenced by the brush tethered to a nanopatterned surfaces. In this work, we use DPD method to explore spontaneous formation of nanostructured morphologies in the case of a two-component fluid confined in slit-like pores. The two identical pore walls are decorated by stripes of tethered chains. We are interested whether the structure imposed by patterned tethered brush is propagated into the pore interior. We also study the mutual influence of the brush and confined binary mixture, on their respective structures, depending on the pore and stripes geometry. To our best knowledge no similar research has been undertaken so far. We also present sketch phase diagram for the observed morphologies depending on the system geometry. However, we make no attempt to locate precise phase boundaries separating the different nanostructures, but we rather focus on quantification of various effects of self-assembly including local density and temperature profiles and introducing appropriate characteristics. The paper is organized as follows. In Sec. II we concentrate on the description of the model and simulation method emphasizing the way how the surface interactions are introduced. In Sec. III we analyze different morphologies and build the sketch phase diagram for them. Section IV is devoted to the description and discussion of the microstructure of morphologies including a number of quantitative characteristics. The summary of the results is presented in Sec. V.

II. MODEL AND SIMULATION METHOD

To model the behavior of one- and two-component fluids in a pore with patterned walls, modified with tethered chains, we consider simulation box of dimensions L_x, L_y, and L_z. The periodic boundary conditions are applied along X and Y axes and two impenetrable walls are introduced in Z direction, namely, at $z = 0$ and at $z = L_z \equiv d$, where d is the pore size. Each wall is divided into stripes of equal width, w, alternating those with and without polymers attached, see Fig. 1 (top frame). The stripes are placed "in-phase" at both walls. The system is homogeneous along the Y axis. The rest of the pore interior is filled by single beads, representing the fluid components.

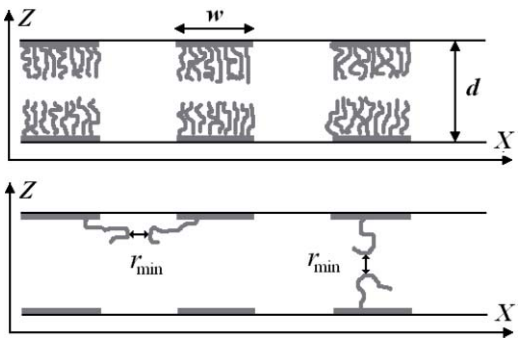

FIG. 1. Geometry of the pore with "in-phase" stripes of polymer chains on both surfaces; the pore size is d and the stripes width is w (top frame). Illustration of chain-chain minimum distances r_{min} for adjacent stripes along X axis and for opposite stripes along Z axis (bottom frame).

We use the DPD approach, as discussed by Groot and Warren,[53] which has been extended to the case of the presence of an impenetrable surface and grafted polymer chains. Polymer chains are formed out of beads linked via harmonic bonds, the bonding force is

$$\mathbf{F}_{ij}^{B} = -kr_{ij}\hat{\mathbf{r}}_{ij}\,, \tag{1}$$

where $r_{ij} = |\mathbf{r}_{ij}|$, $\mathbf{r}_{ij} = \mathbf{r}_i - \mathbf{r}_j$ is the vector connecting the centers of ith and jth beads, $\hat{\mathbf{r}}_{ij} = \mathbf{r}_{ij}/r_{ij}$ and k is the spring constant. Both polymer and solvent beads are subject to three non-bonded pairwise forces[53]

$$\mathbf{F}_{ij} = \mathbf{F}_{ij}^{\mathrm{C}} + \mathbf{F}_{ij}^{\mathrm{D}} + \mathbf{F}_{ij}^{\mathrm{R}}\,, \tag{2}$$

namely, the conservative $\mathbf{F}_{ij}^{\mathrm{C}}$, dissipative $\mathbf{F}_{ij,}^{\mathrm{D}}$ and random $\mathbf{F}_{ij}^{\mathrm{R}}$ forces,[53]

$$\mathbf{F}_{ij}^{\mathrm{C}} = \begin{cases} a(1-r_{ij})\hat{\mathbf{r}}_{ij}, & r_{ij} < 1, \\ 0, & r_{ij} \geq 1, \end{cases} \tag{3}$$

$$\mathbf{F}_{ij}^{\mathrm{D}} = -\gamma w^{\mathrm{D}}(r_{ij})(\hat{\mathbf{r}}_{ij}\cdot\mathbf{v}_{ij})\hat{\mathbf{r}}_{ij}, \tag{4}$$

$$\mathbf{F}_{ij}^{\mathrm{R}} = \sigma w^{\mathrm{R}}(r_{ij})\theta_{ij}\Delta t^{-1/2}\hat{\mathbf{r}}_{ij}. \tag{5}$$

Here $\mathbf{v}_{ij} = \mathbf{v}_i - \mathbf{v}_j$, $\mathbf{v}_i$ and $\mathbf{v}_j$ are the velocities of the beads, θ_{ij} is Gaussian random variable, $\langle\theta_{ij}(t)\rangle = 0$, $\langle\theta_{ij}(t)\theta_{kl}(t')\rangle = (\delta_{ik}\delta_{il} + \delta_{il}\delta_{jk})\delta(t-t')$. According to Español and Warren,[47] the dissipative and random force amplitudes are interrelated, $w^{\mathrm{D}}(r_{ij}) = (w^{\mathrm{R}}(r_{ij}))^2$ and $\sigma^2 = 2\gamma$, to satisfy the requirement of detailed balance. The frequently used analytical form for $w^{\mathrm{D}}(r_{ij})$ is

$$w^{\mathrm{D}}(r_{ij}) = (w^{\mathrm{R}}(r_{ij}))^2 = \begin{cases} (1-r_{ij})^2, & r_{ij} < 1, \\ 0, & r_{ij} \geq 1. \end{cases} \tag{6}$$

In all equations we used pretty standard parameters assuming the length, mass, time, and energy (expressed via $k_{\mathrm{B}}T^*$) units equal to unity. The bulk number density of beads is $\rho = 3$, the friction parameter is $\gamma = 4.5$, the bond spring constant is $k = 4$. The parameter a in the conservative force defines maximum repulsion between two beads, which occurs at a complete overlap, $r_{ij} = 0$. It is an effective one and depends on density and temperature. We consider two types of beads, A and B. In our simulations we use the following values, $a_{AA} = a_{BB} = 25$ for the beads of the same sort[53] and $a_{AB} = 40$ for unlike beads. The latter value reflects poor miscibility of A and B beads and can be related to the Flory-Huggins parameter.[53] Similar values have been used in a number of previous studies, e.g., in a study of scaling properties of polymer chain[54] and of the phase behavior of branched copolymers.[55]

As it was stated by Visser *et al.*,[56] the mesoscopic modelling of confined systems imposes the following requirements for a wall: (1) impenetrability; no particles are allowed to cross the wall, (2) the wall should not artificially affect the fluid properties in the system, and, if the flows are studied, then (3) no-slip; the wall should impose the correct velocity. Since we are interested in static equilibrium properties only, the requirement (3) is less important in this particular study. To account for the existence of an impenetrable wall, one can use several approaches. For instance, one can consider layers of frozen particles residing on each surface.[37,56,57] However, it was also found that such approach does not guarantee that the conditions (1) and (2) are satisfied. In particular, a lattice structure of the wall made of layers of frozen particles was found to have an impact on the structure of the adjacent regions of fluid.[57]

To avoid this shortcoming we prefer to use the structureless surface potential, the details are given below. Another shortcoming of the frozen beads wall model is that such a wall could be occasionally crossed by some beads, therefore, later the idea of reflecting the particles off the wall was introduced to assure the wall impenetrability.[58] We also exploit this idea but supplement it by additional conservation conditions.

To assure wall impenetrability and to construct a structureless wall we employ the following method. If the ith bead with coordinates $\mathbf{r}_i = \{x_i, y_i, z_i\}$ approaches the surface, e.g., the plane $z = 0$, it starts to interact with an "imaginary" bead that has the coordinates $\mathbf{r}_j = \{x_i, y_i, 0\}$, located on the $z = 0$ surface (similarly for the $z = d$ surface). This interaction has all three contributions given by Eqs. (3)–(5), similarly to the interaction between any two "real" beads in the system. The repulsion of the surface can be tuned by adjusting the parameter of conservative force a_S. In this study, we choose it to be equal to a_{AA} and a_{BB}, namely $a_S = 25$, therefore the surface is equally "good" for both sorts of beads A and B. The condition of total momentum conservation for the bead-wall interaction is applied by the following procedure. The force acquired by each wall due to the interaction with approaching beads is accumulated during the evaluation of forces and is then evenly distributed over all beads inside the simulation box. The effective surface, therefore, is structureless and, thus, it does not introduce any artificial perturbation of the fluid structure near the wall (requirement (2)).

Each polymer chain is grafted by one of its ends to a grafting point. The grafting points are fixed on each wall and are distributed randomly inside the stripes with certain grafting density ρ_g. This value cannot be too high, as, in this case, confined fluid will insufficiently influence the brush behavior. It also cannot be too small because, in this case, the brush will reduce into a set of almost independent diluted polymer chains. We found reasonable value to be $\rho_g = \rho/3 = 1$ by performing auxiliary simulations. Grafting potential is introduced in a similar spirit to the bonding potential of polymer beads (1). The spring constant for grafting potential is set to the same value, $k_g = k = 4$.

The proposed approach to account for the surface potential yields the following integrator. We start from the positions $\mathbf{r}_i(t)$, velocities $\mathbf{v}_i(t)$, and reduced forces $\mathbf{f}_i(t) = \mathbf{F}_i(t)/m_i$ at time t and perform the following sequence of steps:

for $i = 1, N$
$\mathbf{v}_i(t + \frac{\Delta t}{2}) = \mathbf{v}_i(t) + \mathbf{f}_i(t)\frac{\Delta t}{2}$,
$\mathbf{r}_i(t + \Delta t) = \mathbf{r}_i(t) + \mathbf{v}_i(t + \frac{\Delta t}{2})\Delta t$,
apply PBC in X, Y
if $(z_i(t + \Delta t) < 0)$ { (*check for crossing* $z = 0$)
  $v_i^z(t + \frac{\Delta t}{2}) = v_i^z\left(t + \frac{\Delta t}{2}\right) - 2z_i(t + \Delta t)/\Delta t$,
  $p_S^z = p_S^z + m_i[2z_i(t + \Delta t)/\Delta t]$,
  $z_i(t + \Delta t) = -z_i(t + \Delta t)$,
else if $(z_i(t + \Delta t) > d)$ { (*check for crossing* $z = d$)

$$
\begin{aligned}
&v_i^z\left(t+\tfrac{\Delta t}{2}\right) = v_i^z\left(t+\tfrac{\Delta t}{2}\right) - 2(z_i(t+\Delta t)-d)/\Delta t,\\
&p_S^z = p_S^z + m_i[2(z_i(t+\Delta t)-d)/\Delta t],\\
&z_i(t+\Delta t) = 2d - z_i(t+\Delta t).\\
&\}\\
&\mathbf{v}_i'(t+\Delta t) = \mathbf{v}_i(t+\tfrac{\Delta t}{2}) + 0.3\,\mathbf{f}_i(t)\tfrac{\Delta t}{2}\\
&(\textit{estimate for } \mathbf{v}_i(t+\Delta t)),\\
\}&\\
&\mathbf{p}_S = (0,0,p_S^z)\ (\textit{wall momentum vector})\\
&\text{calculate } \mathbf{f}_i(t+\Delta t) \text{ based on } \mathbf{r}_i(t+\Delta t), \mathbf{v}_i'(t+\Delta t)\\
&\text{for } i = 1, N\\
&\quad \mathbf{v}_i(t+\Delta t) = \mathbf{v}_i(t+\tfrac{\Delta t}{2}) + \mathbf{f}_i(t+\Delta t)\tfrac{\Delta t}{2} + \tfrac{1}{N}\mathbf{p}_S/m_i,\\
&\text{calculate kinetic energy, temperature, and pressure at } t+\Delta t.
\end{aligned}
$$

This integrator is an extension of modified velocity-Verlet algorithm of Groot and Warren[53] for the presence of a surface. In particular, the beads are reflected off the wall if they cross the simulation box boundaries at $z = 0$ or $z = d$. The momentum transferred to the wall, $\mathbf{p}_S = (0, 0, p_S^z)$, is collected at each reflection event and is redistributed evenly among the beads when $\mathbf{v}_i(t + \Delta t)$ is evaluated. This procedure, alongside with the way the bead-wall interactions are treated (see above), ensures conservation of each component of the total momentum with the accuracy of at least 10^{-8}. The range of system sizes is from $N = 64\,000$ up to 3.24×10^6 depending on the pore geometry. The simulations have been performed in NVT ensemble with the timestep of $\Delta t = 0.04$.

Morphologies are visualised via density grid. Simulation box is splited into a grid of cubic cells with linear dimension of 0.75−2.0 depending on the box size. Local densities for A beads $\rho_A(x, y, z)$ and for B beads $\rho_B(x, y, z)$ are evaluated inside each cell where the cell coordinates are (x, y, z). These are averaged over the coordinates files for which the morphology stabilizes itself (typically, the last $(2 - 5) \times 10^4$ simulation steps). Density difference, $\rho_{AB}(x, y, z) = \rho_A(x, y, z) - \rho_B(x, y, z)$ is colour coded with bluish tint for positive (mostly A beads) and reddish tint for negative (mostly B beads) values. The interface regions $\rho_{AB}(x, y, z) \sim 0$ are displayed in gray. Most morphologies are best seen in 3D representation for which purpose we space-fill bluish and gray cells only and show reddish cells as dots.

For the morphologies that are translationally invariant along the Y axis the data have been averaged along this direction. If a given morphology is additionally translationally invariant in other direction (e.g., X), then the densities have been also averaged in that direction to enable plotting the 2D density profiles. The kinetic energy and hence the local temperature, k_BT, has been evaluated in each cell for each sort of beads using the same symmetry considerations as for the local densities.

III. DIAGRAM OF MORPHOLOGIES

We consider a wide range of pore sizes $d \in [13.333, 50]$ and stripe widths $w \in [4, 140]$. In majority of cases the number of stripes is $N_{\text{str}} = 4$, except for the cases of $d = 30$, $w = 90$ and of $d = 50$ (for all values of w), where $N_{\text{str}} = 3$ due to much increased system size. The dimensions of the box are: $L_x = 2N_{\text{str}}w$, $L_y = 50$ (in most cases except the largest values of d and w, where it is $L_y = 40$) and $L_z = d$. The polymer beads are of type A, whereas the interior of the pore is filled by a binary mixture of beads A and B. In all cases the mixture of all beads is symmetric in the sense that the total numbers of beads A and B are the same

$$N_A^p + N_A^s = N_B^s, \tag{7}$$

where the superscript p or s denotes polymer or solvent, respectively, while the subscript indicates the bead sort, A or B. For fixed bulk, $\rho = 3$, and grafting, $\rho_g = 1$ densities, polymer length $L = 20$, and stripes geometry one can calculate the minimum pore size d_{min}, at which no solvent beads of sort A are present, namely,

$$
\begin{aligned}
&N_A^p = \frac{1}{2}N_{\text{tot}}, \quad 2\rho_g\frac{L_x}{2}L_yL = \frac{1}{2}\rho L_xL_yd_{\text{min}},\\
&d_{\text{min}} = 2\,\frac{\rho_g}{\rho}\,L \approx 13.333.
\end{aligned}
\tag{8}
$$

In this case one has a patterned polymer brush in a bad solvent and the ratio of the beads $N_A^p : N_A^s : N_B^s$ is $1 : 0 : 1$.

For this specific pore size, $d = 13.333$, we consider the systems with the stripe widths ranging from $w = 4$ to $w = 30$. Two distinct morphologies have been observed. For narrow stripes, $w < 5$, the lamellar structure has been found to be stable. In this case, the polymer brushes cover both pore walls. Instantaneously, the solvent B is demixed and forms a wide layer at the pore center (see Fig. 2, top frame, on the left). For $w \geq 5.3$ pillar morphology develops: the opposite stripes of brushes merge across the pore. This structure does not change with further increase of w (see Fig. 2, bottom frame). In a narrow interval of stripe widths, $w \in [5, 5.2]$ one observes "a mixture" of lamellar and pillar morphologies (Fig. 2, top frame, on the right).

This sequence of morphologies can be explained by the competition of various contributions to the free energy. These are, the free energy of demixing, $\mathcal{F}_{\text{dem}}$, and the conformational free energy of polymer chains, $\mathcal{F}_{\text{conf}}$. The first one can be estimated from the interfacial tension between A-rich and B-rich regions. Assuming it to be constant, $\mathcal{F}_{\text{dem}}$ is proportional to the surface area $\mathcal{A}$ between A-rich and B-rich regions. This area is equal to $\mathcal{A}_{\text{lam}} = 2L_xL_y = 4N_{\text{str}}wL_y$ for lamellar and $\mathcal{A}_{\text{pil}} = 2N_{\text{str}}L_yL_z = 2N_{\text{str}}L_yd$ for pillar morphology. Both areas (and thus $\mathcal{F}_{\text{dem}}$) coincide at $w = d/2 \approx 6.67$. The transition, however, occurs at smaller values of $w_{\text{lp}} \in [5, 5.2]$, where the mixture of both morphologies is

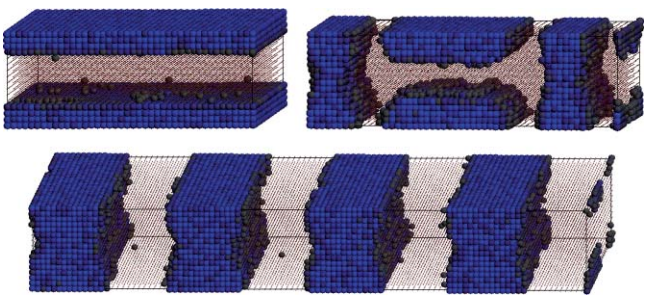

FIG. 2. Colour-coded density grid (for details, see the text) $\rho_{AB}(x, y, z)$ for morphologies: lamellar ($w = 4$, top frame, on the left), mixed ($w = 5.1$, top frame on the right), and pillar ($w = 10$, bottom frame). In all cases $d = 13.333$.

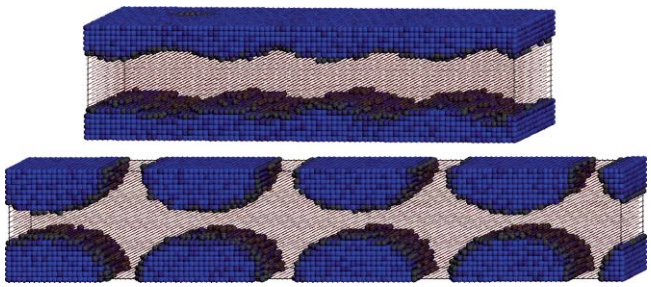

FIG. 3. Additional morphologies observed in pores of the size $d = 20$: a modulated lamellar ($w = 9$, top frame) and separated droplets ($w = 13$, bottom frame).

observed (see, Fig. 2, top frame on the right). To explain this, the $\mathcal{F}_{\text{conf}}$ should be taken into account. It depends on average conformation of polymer chains and is addressed in Sec IV. Moreover, a more precise evaluation of $\mathcal{F}_{\text{dem}}$ requires also taking into account the effect of the interface curvature on the interfacial tension.

For the pore size of $d = 20$ the system contains A and B beads at the following ratio $N_A^p : N_A^s : N_B^s = 2 : 1 : 3$. For $w < 8$ we observe lamellar morphology, similar to that found for $d = 13.333$ and $w < 5$. In this case the beads of solvent A are mixed well with the polymer beads in the polymer-rich layers that cover both surfaces. With an increase of w new morphologies are observed. The first one is spatially modulated lamellar structure with sinusoidally shaped layers formed by the beads of type A. It occurs for $w \in [8, 9]$ (see Fig. 3, top frame). The second one is the separated droplets morphology that takes place for $w \in [12, 18]$ (see Fig. 3, bottom frame).

For wider stripes, $w \in [20, 30]$ a pillar morphology is found. Its structure looks similar to that observed for the pore size of $d = 13.333$ (cf. Fig. 2, bottom frame). However, for still wider stripes, $w > 30$, one observes reentrant droplets morphology that has been already found for $8 < w < 12$. Solvent A beads do not diffuse from the polymer-free regions into the gaps between the droplets to promote formation of pillars. More details on the crossover between pillar and droplets morphologies is given in Sec. IV.

For $d = 20$ and $w > 50$ the increasing amount of solvent A beads and the enlarging polymer-free regions enable a spontaneous formation of domains of solvent A beads in polymer-free regions. To study this process in detail we performed simulations at wide range of stripe widths, namely, for $w = 80, 90, 100, 120$, and 140. In all cases from one to three cylindrical domains of solvent A beads were formed in polymer-free regions. Cylinders span across the pore.

The kinetics of their formation is similar in all cases mentioned above and is illustrated by snapshots of one single polymer-free region for the case of $d = 20$ and $w = 100$ in Fig. 4. At first stages (at times $t \approx 100$–200) solvent A beads nucleate into droplets. Many of them are of semispherical shape and are attached to one surface of the pore. This is explained by the surface potential applied, which uses the concept of a single repulsive surface particle and does not employ an integration over the surface particles (see, Sec. II). Therefore, for $a_S = a_{AA} = a_{BB}$, the surface potential is less

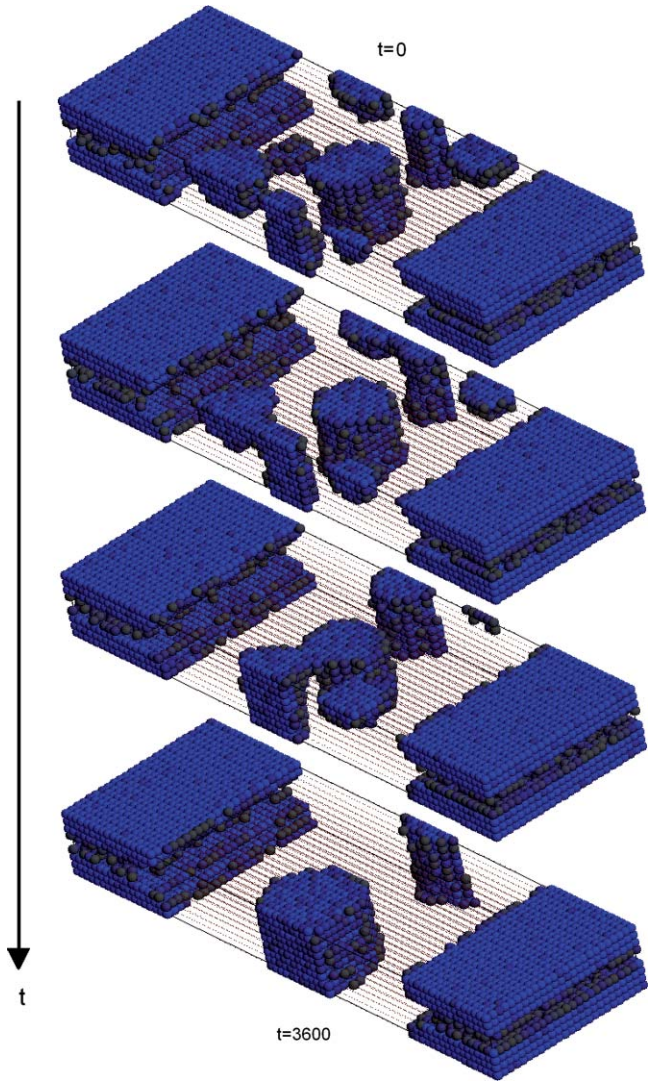

FIG. 4. Nucleation kinetics of solvent A domains in polymer-free stripes for $d = 20$, $w = 100$. Mixture of semidroplets and cylinders (topmost frame, time $t = 2000$); merge of semidroplets and cylinders (second from the top, $t = 2600$); merge of two cylinders (third from the top, $t = 3000$); final single cylinder domain (bottom frame, $t = 3600$).

repulsive than it would be for a wall of beads. This causes nucleation of beads A into semispheres on the surfaces easier. At later stage, $t \approx 1000$–2000 some droplets merge into cylinders spanning across the pore (see the second frame from the top in Fig. 4). Other droplets merge gradually with the nearest cylindrical domains, as shown in the same figure. Some droplets diffuse into gaps between droplets at opposite surfaces partly filling the latter. We found that when simulations last longer than $t = 8000$, no droplets can persist. The number of cylindrical domains vary from one to three and depends on random factors during nucleation. Merging two neighboring cylindrical domains into a single one is shown in Fig. 4 (two bottommost frames). Slow diffusion of cylinders hinders their ability to merge, or, at least, their merging would require simulation runs much longer than employed in this study. The fraction of A beads f_A in polymer-free regions ranges from $f_A \approx 0.12$ for $w = 80$ to $f_A \approx 0.25$ at $w = 120 - 140$. One may try to link these values to the typical fractions at which

FIG. 5. Spontaneous formation of cuboidal domains of solvent A beads in polymer-free stripes, $d = 30$ and $w = 90$.

a minor component forms cylindrical domains in the case of diblock copolymer systems.[55]

Let us consider now larger pore of the size of $d = 30$. In this case the proportions of beads are: $N_A^p : N_A^s : N_B^s = 1 : 1.25 : 2.25$ and the sequence of morphologies is similar as in the case of $d = 20$. One observes lamellar morphology for $w \leq 10$, modulated lamellar morphology at $w \approx 15$ and separate droplets morphology for $w \in [25, 40]$. No pillar morphology has been found, though, as for $w \geq 50$, the bulk-like phase separation is brought into play, similarly, as in the case of $d = 20$ and $w > 30$. For $w = 60$ and $w = 70$ some domains of solvent A remain separated while others diffuse into gaps between droplets at opposite surfaces. An interesting effect found is that at $w = 90$ stand-alone cuboidal domains of solvent beads A are formed right in the center of each polymer-free region (see, Fig. 5). The fraction of A that beads f_A in these regions is $f_A \approx 0.3$, which may be the factor deciding about the cuboidal domain shape. The situation in Fig. 5 contrasts with the already discussed case of one to three cylindrical domains formed inside the pore of the size of $d = 20$.

With further increase of the pore size to $d = 50$ (the proportions of beads are now $N_A^p : N_A^s : N_B^s = 1 : 2.75 : 3.75$) the self-assembly of the system is dominated by bulk effects. One observes the formation of separate droplets and of lamellar and pillar fragments. Typical case of $d = 50$ and $w = 30$ is shown in Fig. 6.

The intervals of stability for the morphologies for various pore sizes, d, and stripe widths, w, can be summarized into a sketchy diagram, shown in Fig. 7. Lamellar and pillar morphologies appear along respective axes. The breadth of appropriate regions is of the order of chain length, $L = 20$. At larger, but still moderate values of d and w the droplets morphology is found (dashed area in Fig. 7 marked as "DROPLETS"). For larger values of d and w additional number of solvent beads A are available. As far as the droplets are already saturated with solvent A beads, these additional A beads cannot enter the interior of droplets. Therefore, they self-assemble into bulk structures inside the polymer-free regions (cross-dashed area in Fig. 7 marked as "DROPLETS + BULK").

At the end of this section we discuss how the case of stripes built of chains composed of $L = 20$ beads considered so far compares with the case of "atomic" stripes with $L = 1$. Our simulations have been carried out for the same set of pore sizes as for $L = 20$ and for a range of stripe widths $w \in [5, 90]$. The total number of grafted beads (denoted as N_A^p for the sake of compatibility) is now much smaller as compared with the number of solvent beads, N_A^s and N_B^s. The ratios of particular beads range from $N_A^p : N_A^s : N_B^s = 1 : 19 : 20$ for $d = 13.333$ to $N_A^p : N_A^s : N_B^s = 1 : 74 : 75$ for $d = 50$. Therefore, the confined binary mixture of solvent A and solvent B beads can be considered as almost exactly symmetric mixture.

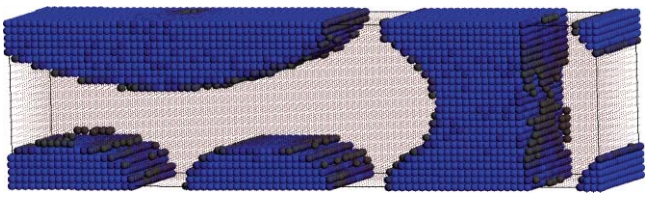

FIG. 6. Domination of bulk effects for $d = 50$. Fragments of various morphologies are shown for a typical case of $w = 30$.

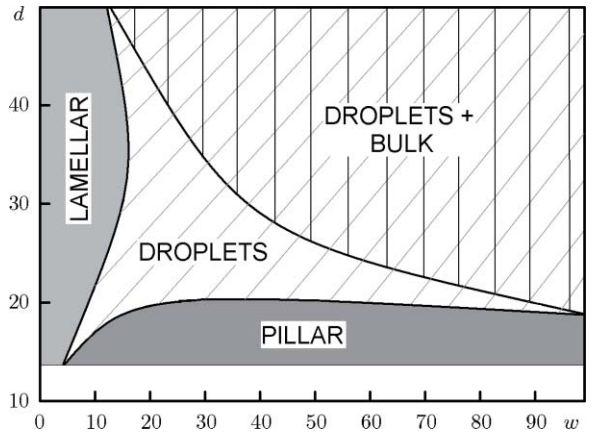

FIG. 7. Sketch for the diagram of morphologies depending on pore sizes d and on stripes widths w.

The main outcome of our simulations for $L = 1$ can be summarized in a rather brief statement. For $w \ll d$, the binary mixture of A and B solvent beads does not "see" the fine structure of the stripes and separate similarly as in the bulk case. A-rich and B-rich regions of random shape are formed.[59] For instance, for $d = 13.333$, two large domains, either cuboidal (for $w = 4$) or cylindrical (for $w = 6$) in shape develop (see, Fig. 8, top frame). When w becomes compatible with the pore size d, then the phase separation of the species begins to be driven by the stripes geometry. Indeed, for $d = 20$ and $w = 20$ (Fig. 8, middle frame) usual pillar morphology is formed. Obviously, for different ratio $N_A^p : N_A^s : N_B^s$ the observed morphology can be different. For the values of w significantly larger than the pore size, d, the bulk-like type phase separation between solvent species is observed again,

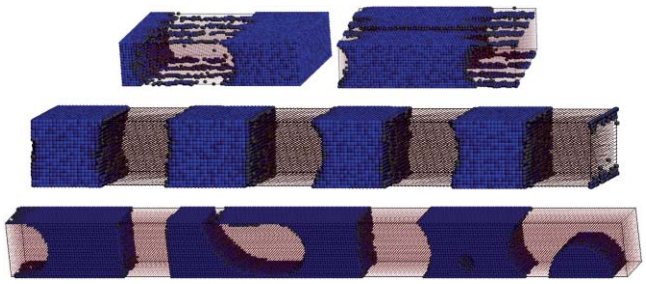

FIG. 8. Microphase separation of A and B beads for $L = 1$ stripes at various w. Top frame – bulk-like effects at $w \ll d$, the cases of cuboidal ($d = 13.333$, $w = 4$, on the left) and cylindrical ($d = 13.333$, $w = 6$, on the right) domains are shown. Middle frame – stripe-driven formation of pillar morphology at $w \sim d$ (the case $d = 20$, $w = 20$ is shown). Bottom frame – reentrant bulk-like microphase separation at $d = 50$ and $w = 90$.

TABLE I. Morphologies observed for $d = 13.333$ and for different stripes widths w and metric properties of polymer chains defined by Eqs. (11)–(14). Estimated standard deviation for $G_{\alpha\alpha}$ does not exceed 1%.

w	G_{xx}	G_{yy}	G_{zz}	σ_1^2	σ_2^2	σ_3^2	R_g	R_h	Morphology
4.0	1.20	1.09	**0.63**	**2.19**	0.54	0.20	1.71	1.59	Lamellar
5.0	1.34	1.06	**0.75**	**2.38**	0.56	0.20	1.77	1.62	Mixed
5.1	0.99	1.04	**1.63**	**2.90**	0.56	0.19	1.91	1.68	Mixed
5.2	1.19	1.04	**1.22**	**2.69**	0.56	0.20	1.86	1.65	Mixed
5.3	0.73	1.04	**2.31**	**3.33**	0.56	0.19	2.02	1.73	Pillar
10.0	0.88	1.03	**2.55**	**3.67**	0.58	0.20	2.11	1.78	Pillar
30.0	0.99	1.03	**2.65**	**3.88**	0.60	0.20	2.16	1.81	Pillar

as in the case of $d = 50$ and $w = 90$ (see Fig. 8, bottom frame). Similarly, as in the case of $w \ll d$ the typical domain size is incommensurate with the characteristic lengthscale w and, as the result, the bulk effects are prevailing. The case of "atomic" stripes can be related to the upper right corner of the diagram depicted in Fig. 7.

IV. MICROSTRUCTURE OF MORPHOLOGIES

Let us concentrate now on the microstructure of the morphologies that have been classified in Sec. III. Anisotropy in spatial distribution of the beads of each kth polymer chain can be characterized by the components of the gyration tensor, defined in a standard way

$$G_{\alpha\beta}^{[k]} = \frac{1}{N}\sum_{i=1}^{N}\left(r_{i,\alpha}^{[k]} - R_{\alpha}^{[k]}\right)\left(r_{i,\beta}^{[k]} - R_{\beta}^{[k]}\right). \tag{9}$$

Here α, β denote Cartesian axes, $r_{i,\beta}^{[k]}$ are the positions of individual monomers, and $\mathbf{R}^{[k]}$ is the center of mass position of the kth chain. The trace of this tensor is equal to squared radius of gyration, $(R_g^{[k]})^2$, and its eigenvalues are $(\sigma_\alpha^{[k]})^2$, where $\sigma_\alpha^{[k]}$ are semiaxes of the equivalent ellipsoid for the kth molecule. The inverse hydrodynamical radius $R_h^{[k]}$ can be evaluated from the following relation:

$$\frac{1}{R_h^{[k]}} = \frac{1}{N^2}\sum_{i\neq j}\frac{1}{r_{ij}^{[k]}}, \tag{10}$$

where r_{ij} is the distance between ith and jth bead belonging to kth chain. The quantities $G_{\alpha\beta}^{[k]}$, $(\sigma_\alpha^{[k]})^2$, $(R_g^{[k]})^2$, and $1/R_h^{[k]}$ are averaged over polymer chains and over the time trajectory in equilibrium morphology of the system. The final metric properties are computed in the following way:

$$R_g = \sqrt{\left\langle \left(R_g^{[k]}\right)^2\right\rangle_{k,t}}, \tag{11}$$

$$\frac{1}{R_h} = \left\langle 1/R_h^{[k]}\right\rangle_{k,t}, \tag{12}$$

$$G_{\alpha\beta} = \left\langle G_{\alpha\beta}^{[k]}\right\rangle_{k,t}, \tag{13}$$

$$\sigma_\alpha^2 = \left\langle \left(\sigma_\alpha^{[k]}\right)^2\right\rangle_{k,t}. \tag{14}$$

We employed the following ordering for σ_α, $\sigma_1 > \sigma_2 > \sigma_3$. These properties obtained for the pore sizes $d = 13.333$ and $d = 20$ are given in Tables I and II, respectively.

Let us point out some general observations first. The G_{yy} component of the gyration tensor is almost constant for all the morphologies listed in Tables I and II which can be attributed to the uniformity of the system along the Y axis. The smallest squared semiaxis of the equivalent ellipsoid, σ_3^2, and, to large extend, the medium one, σ_2^2, are also found to be almost constant. The characteristic ratio σ_2^2/σ_3^2 ranges from 2.7 to 3.1 which is quite close to 2.5, i.e., to the ratio for the case of an ideal chain.[60] This indicates that the average chain conformation in the plain perpendicular to its longest axis is almost Gaussian.

The principal metric peculiarity in the lamellar morphology observed for $d = 13.333$ is the oblate shape of polymer

TABLE II. Morphologies observed for $d = 20$ and for different stripes widths w and metric properties of polymer chains defined by Eqs. (11)–(14). Estimated standard deviation for $G_{\alpha\alpha}$ does not exceed 1%.

w	G_{xx}	G_{yy}	G_{zz}	σ_1^2	σ_2^2	σ_3^2	R_g	R_h	Morphology
5.0	**1.29**	1.09	**1.19**	**2.74**	0.62	0.21	1.89	1.70	Lamellar
7.0	**1.50**	1.09	**1.21**	**2.97**	0.62	0.21	1.95	1.73	Lamellar
8.0	**1.57**	1.08	**1.22**	**3.04**	0.63	0.21	1.97	1.75	Mod.lam.
9.0	**1.68**	1.06	**1.28**	**3.19**	0.63	0.21	2.00	1.76	Mod.lam.
10.0	**1.53**	1.05	**1.52**	**3.27**	0.63	0.21	2.03	1.77	Trans.
12.0	**1.11**	1.07	**2.18**	**3.52**	0.63	0.21	2.09	1.80	Droplets
18.0	**1.14**	1.06	**2.72**	**4.09**	0.63	0.20	2.22	1.85	Droplets
20.0	**1.06**	1.04	**3.22**	**4.49**	0.62	0.20	2.31	1.88	Pillars
30.0	**1.02**	1.03	**3.97**	**5.21**	0.61	0.20	12.45	1.93	Pillars
50.0	**1.04**	1.02	**4.00**	**5.24**	0.62	0.20	2.46	1.94	Pillars + cyl.
90.0	**1.05**	1.03	**3.42**	**4.67**	0.62	0.20	2.34	1.90	Dropl. + cyl.

chains. Indeed, G_{zz} is approximately half of G_{xx} or G_{yy} values (see Table I). Moreover, the values of G_{xx} or G_{yy} are similar what indicates that the system in lamellar morphology is at least partially uniform along the X direction. Therefore, the formation of an uniform layer near the surface occurs by bending chains along the X axis to fill-in the polymer-free stripes. This effect is well detectable even when one averages over all the chains of each stripe (as we did in this study), and is expected to be more pronounced if only the boundary chains of each stripe are selected. One should mention that the preservation of the lamellar (or modulated lamellar) morphology with the increase of w requires more stretch of the chains along the X direction, this is clearly indicated by the larger values of G_{xx} at $w = 7 - 9$ as compared to the case of $w = 5$ for the pore size $d = 20$ (Table II).

In the pillar morphology the situation is reversed. G_{zz} is about 2.5 times larger than either G_{xx} or G_{yy} indicating that the chains are stretched across the pore. Their shape is pronouncedly prolate as follows from the values of the largest semiaxes σ_1. The characteristic ratio σ_1^2/σ_3^2 increases from about 11 for lamellar morphology ($w = 4$) to 17.5 for early pillar morphology ($w = 5.3$) up to 19.4 for well developed pillar morphology ($w = 30$). This indicates essential departure from the regime of Gaussian chain for which this ratio is ~ 11.8.[60] It is evident that these conformational changes are the result of the competition between free energies $\mathcal{F}_{\text{dem}}$ and $\mathcal{F}_{\text{conf}}$ introduced above. In pillar morphology, the gain from the first contribution due to merging of brushes is bigger than the loss from the second one, due to deformation of the chains.

In the lamellar morphology observed at pore size of $d = 20$, the distribution of chains in space is more isotropic ($G_{xx} \approx G_{yy} \approx G_{zz}$). G_{xx} is slightly larger than two other components and exhibits a maximum in modulated lamellar morphology (for $w \in [8, 9]$). This indicates extension of chains along the X axis close to the surfaces in order to fill-in the polymer-free stripes. Additional gain in $\mathcal{F}_{\text{dem}}$ is achieved by filling these regions also by the solvent A beads. This compensates for the the loss in $\mathcal{F}_{\text{conf}}$, similarly to the case discussed above. With the increase of w, a sharp decrease of the value of G_{xx} occurs at $w \approx 10$, where G_{xx} drops down to about 1 and stays constant with further increase of w. Pillar morphology for the pore size $d = 20$ demonstrates even larger anisotropy in gyration tensor components than that found for $d = 13.333$. In fact, the values of G_{zz} are up to four times larger than the values of G_{xx} or G_{yy} (see Table II).

To characterize both lamellar and pillar morphologies and the transition between them quantitatively, we analyzed the measure of merging between both adjacent stripes within the same surface plane and between stripes placed at opposite pore walls. Let us consider the case of adjacent stripes within the same wall first. We built a 3D grid of cells and then the loop over all pairs of chains, m and n is performed providing that the chains belong to adjacent stripes. The inner loop runs then over all the (i, j) pairs of beads, where the bead i belongs to mth chain and the bead j belongs to nth chain. From all of these pairs we select only those for which (y_i, z_i) and (y_j, z_j) belong to the same grid cell in the YZ plane. All the distances r_{ij} between such pairs are calculated and the minimum one, r_{min}, is selected to construct the histogram of the distribution, $\rho_x(r_{\text{min}})$. Similar procedure is used to evaluate the histogram $\rho_z(r_{\text{min}})$ of the shortest distances between chains located within the stripes at opposite walls. The definition for the chain-chain minimum distance, r_{min}, in both X and Z directions is illustrated in Fig. 1 (bottom frame).

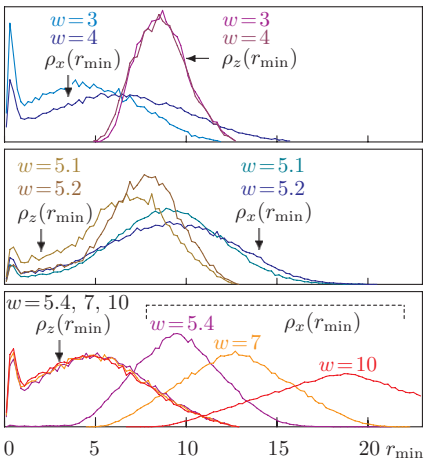

FIG. 9. Distributions of the chain-chain shortest distances r_{min} for the chain pairs from adjacent stripes on the same surface, $\rho_x(r_{\text{min}})$, and for the chain pairs from opposite stripes in Z direction, $\rho_z(r_{\text{min}})$. Top frame – lamellar morphology, bottom frame – pillar morphology, middle frame – transitional mixed morphology. The pore size is $d = 13.333$.

The histograms for $\rho_x(r_{\text{min}})$ and $\rho_z(r_{\text{min}})$ in lamellar and pillar morphologies, as well as for transitional mixed morphology for $d = 13.333$ are shown in Fig. 9. In the case of lamellar morphology (top frame in Fig. 9), one observes high peak of $\rho_x(r_{\text{min}})$ at small distances indicating merging adjacent stripes. The opposite stripes are separated by a distance of at least 5 and the average distance between them equals to about 8.5, as indicated by the plot of $\rho_z(r_{\text{min}})$. In the case of pillar morphology (bottom frame in Fig. 9) the situation is reversed, as clearly indicated by high values of $\rho_z(r_{\text{min}})$ at small distances. The distributions are independent on w. The separation of adjacent layers along X has a maximum at approximately $2w$. The case of transitional mixed morphology for $w = 5.1$ and 5.2 is shown in the middle frame of Fig. 9. The shape of both distributions indicates partial merging of some adjacent and some opposite stripes, supporting the snapshot shown in Fig. 2 (top frame, on the right).

The distributions of chain-chain minimum distances $\rho_x(r_{\text{min}})$ and $\rho_z(r_{\text{min}})$ for the modulated lamellar morphology and droplets morphology for $d = 20$ are shown in Fig. 10. One should note that the polymer chains overlap only

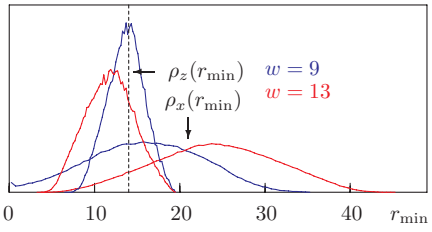

FIG. 10. Distributions similar to those displayed in Fig. 9. Modulated lamellar (at $w = 9$) and separate droplets (at $w = 13$) morphology are shown, the pore size is $d = 20$.

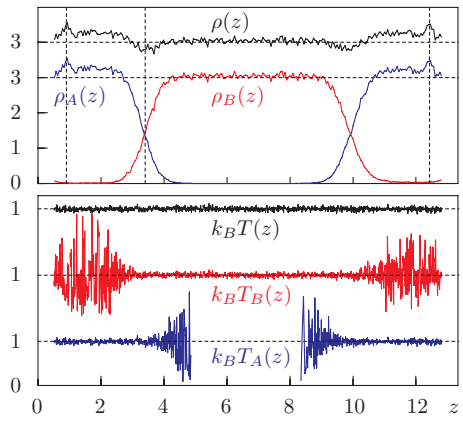

FIG. 11. Local density and local temperature profiles for lamellar morphology at pore size $d = 13.333$ and stripe width $w = 4$. Bead sorts A, B are marked by subscripts and coloured lines, $\rho(z)$ and $k_BT(z)$ stand for the total density and temperature profiles, respectively.

little along the X axis in modulated lamellar morphology (as compared to lamellar morphology for $d = 13.333$, Fig. 9). This indicates that much filling of the lamellae is done by the solvent A beads. This behavior is discussed below in terms of the density profiles. The distributions shown in Fig. 10 for $w = 13$ indicate complete separation of droplets in both directions.

Let us consider now the local densities and local temperatures. The symmetry of lamellar morphology, observed for $d = 13.333$ and $w = 4$, allows us to average local properties over the X axis and build density and temperature profiles only in Z direction. They are abbreviated as $\rho_A(z)$, $\rho_B(z)$, and $\rho(z)$ (for total density) and $k_BT_A(z)$, $k_BT_B(z)$, and $k_BT(z)$ (for average temperature), respectively. We show them in Fig. 11. The regions $z < 0.5$ and $z > 12.833$ are excluded from the plots because beads cannot approach the surface closer than by 0.5. In the top frame of Fig. 11, one can observe the effect of microphase separation of A and B species. The profiles quantify the snapshot shown on the left of the top frame of Fig. 2. At the distances of about 0.9 from both surfaces one observes density peaks due to grafting of the first bead of each chain. One can also see the total density drop in the regions where the densities of A and B species are equal ($z \approx 3.4$ and $z \approx 9.9$). This is explained by strong repulsion of A and B beads. No anomalies of the total density are observed near both surfaces which confirms the validity of the applied integrator.

The local temperature profiles for the lamellar morphology (bottom frame of Fig. 11) indicate good conservation of temperature (equal to 1.0) in both polymer-rich and solvent B rich regions. Large fluctuations of local temperature of polymer beads in solvent B region and *vice verse* result from poor statistics due to insufficient number of beads in these regions. One should stress that no anomalies for the local temperature near the walls are observed.

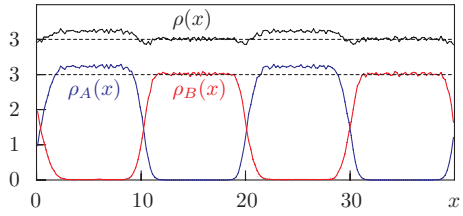

FIG. 12. Local density profiles for pillar morphology for the pore size $d = 13.333$ and for the stripe width $w = 10$. The notations are the same as in Fig. 11.

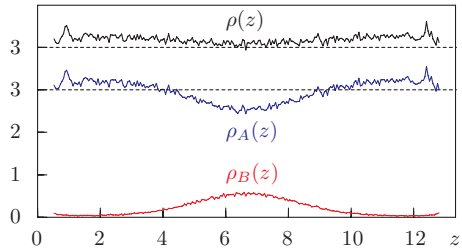

FIG. 13. Local density profiles calculated along Z axis within slab regions as explained in the text. The case of "strong" pillar morphology in the pore of the size $d = 13.333$ and stripe width $w = 10$.

Similar profiles can be built for pillar morphology that has been observed for $d = 13.333$ and $w = 10$. In this case the local properties are averaged in Z direction and the following profiles along X axis can be evaluated: $\rho_A(x)$, $\rho_B(x)$, $\rho(x)$, $k_BT_A(x)$, $k_BT_B(x)$, and $k_BT(x)$. The behavior of these profiles is quantitatively similar to that in Fig. 11, but now the modulation of the local properties takes place along the X axis. In Fig. 12, we show only local density profiles for the sake of brevity. The behavior of the local temperature is similar as in the case of Fig. 11 with large fluctuations of partial temperatures within low local density regions.

Visual inspection of pillars formed during simulation reveals various levels of their overlap, ranging from touching droplets ("weak" pillars) up to highly developed "strong" pillars with meniscus-like sides (see, e.g., bottom frame in Fig. 2). The solvent A beads appear to mix quite uniformly with the polymer beads. To quantify the "quality" of pillar morphology we compute the density profiles within pillars, $\rho_A(z)$, $\rho_B(z)$, and $\rho(z)$. They were evaluated inside the slab regions spanning over entire range in Y and Z directions and restricted to the intervals $x \in [0, w]$, $x \in [2w, 3w]$ and so on along the X axis. The profiles are then averaged over all slab regions. Normalized difference between the densities in the middle of the pore, $\Delta\rho = (\rho_A(\frac{d}{2}) - \rho_B(\frac{d}{2}))/\rho(\frac{d}{2})$, can be considered as the order parameter for the pillar morphology.

The result for the pore of $d = 13.333$ and for $w = 10$ is shown in Fig. 13. It demonstrates a "strong pillar" case

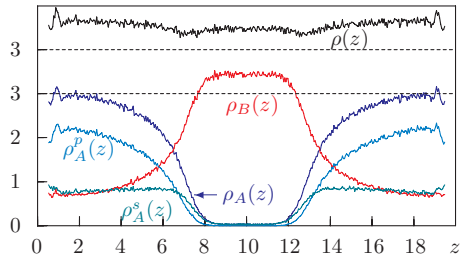

FIG. 14. Local density profiles calculated along Z axis within slab regions as explained in the text. The case of droplets morphology in the pore of the size $d = 20$ and stripe width $w = 13$ is shown here.

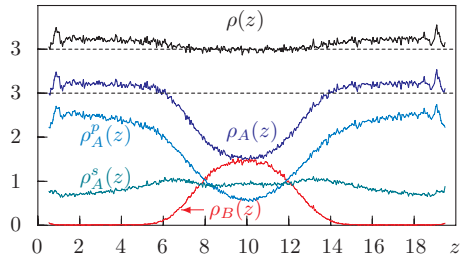

FIG. 15. Local density profiles calculated along Z axis within slab regions as explained in the text. The figure illustrates case of "critical" pillar morphology in the pore of the size $d = 20$ and stripe width $w = 30$.

with the pillar order parameter $\Delta\rho = 0.65$. The breaking continuity within pillars leads to droplets morphology. The pillar order parameter is negative in this case, in particular case of $d = 20$, $w = 13$ it equals $\Delta\rho = -1$, as can be seen in Fig. 14. In this case, we see that the polymer and solvent A are completely excluded from the central region, whereas the solvent B beads are present in droplets with non-zero density $\rho_B^s(x) \approx 0.7$. The solvent A beads profile $\rho_A^s(x)$ is found to follow closely that for the polymer beads, $\rho_A^p(x)$, which is an indication of the sole effect of droplets swelling due to solvent A beads entering polymer rich regions.

Two cases discussed above demonstrate the "strong" pillar and no pillar (droplets) morphologies. The critical case must exist which corresponds to the droplets "touching" each other at the pore center. Pillar order parameter in this case is approximately zero. Such a case is found for $d = 20$ and for $w = 30$ and the density profiles within the slabs are shown in Fig. 15. Solvent A beads spread more or less uniformly across the pore with a slight increase of their local density in the middle of the pore. Polymer beads are also found to spread into the middle of the pore, where they mix well with solvent A beads. As the result, the total densities, $\rho_A(\frac{d}{2})$ and $\rho_B(\frac{d}{2})$ for A and B beads, respectively, are approximately equal bringing the value for the order parameter to $\Delta\rho \approx 0$.

Similar study can be undertaken also for the lamellar morphologies. Especially, the case of non-trivial modulated lamellar morphology (see, Fig. 3, top frame) is of interest. The distribution of polymer and solvent A beads in such morphology can be quantified via the local density profiles within the layers adjacent to both surfaces. In particular, for the case of $d = 20$, $w = 9$ the layers were defined by restricting the Z coordinates to the intervals $z \in [0.5, 6]$ and $z \in [14, 19.5]$.

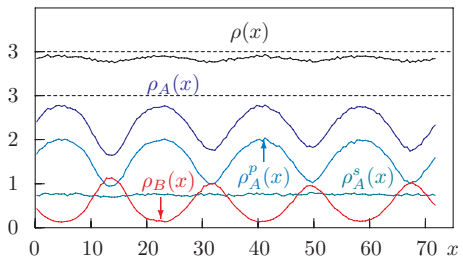

FIG. 16. Local density profiles calculated along X axis within the layers adjacent to the surfaces for modulated lamellar morphology. The pore size is $d = 20$ and stripe width is $w = 9$.

The results are shown in Fig. 16. The shape of the distributions of both polymer and solvent B beads are found to be very close to sinusoidal, whereas the density of solvent A beads is constant across the entire X range. The latter can be explained solely by the fact that the solvent A beads are distributed more densely within the regions of the "valleys" of the sinusoidal shape.

V. SUMMARY

In this work we have employed the DPD simulation technique to study the structure of a binary mixture inside pores modified by stripes of tethered polymer brushes. The solvent has been composed of two types of beads. The beads A have been identical to the beads of chain particles, while the beads of the second sort, B, have been selected in such a way that the bulk A-B mixture exhibits partial mixing. All the calculations have been carried out assuming that the ratio of the total number of A beads to the number of B beads was equal to one. The main aim of our calculations has been to investigate the morphologies that appear inside the pore, depending on the pore size d and the width of the stripes, w. We have constructed a sketch of the diagram of the morphologies and have found that they are governed by (i) the characteristic lengthscale L that is the length of the chains, and by (ii) the fraction of the A-type molecules in the polymer-free regions. For the values of w close to $L/2$ and for $d > d_{\min} \sim L/2$ lamellar morphology was found, while for $w > w_{\text{lp}} \sim L/4$ and $d_{\min} < d < L$, we observed the formation of pillars. Beyond the above regions either droplets or droplets plus bulk-type morphologies have been observed. The self-aggregation within polymer-free stripes seems to be governed by the size of the stripes and by the fraction of A beads within these regions. When this fraction is close to 1/3, cylinders inside polymer-free regions have been formed, while for the fraction close to 1/2 lamellae have developed. In order to characterize the observed morphologies we have calculated several parameters, as the radii of gyration, local densities and histograms of the minimum distances between polymers located in different (within the same plane, as well as at opposing walls) stripes.

It would be of interest to check how the morphologies evolve if the ratio of A to B beads will change and how the morphologies formed under static condition will be preserved – or changed – if the fluid would undergo a pressure-driven flow along the pore axis. The last aspect seems to be particularly interesting, and even important from the practical point of view because the formation of some structures inside the pore "locks" the pore. It would be therefore of interest to check what pressure will be necessary to break the "dams" inside the pore and to open it. These problems are currently under study in our laboratories.

ACKNOWLEDGMENTS

This work was supported by EC under the Grant No. IRSES 268498. S.S. also acknowledges a partial support from the Ministry of Science of Poland under the Grant No. N N204 151237.

[1]R. C. Advincula, W. J. Brittain, K. C. Caster, and J. Ruhe, *Polymer Brushes: Synthesis, Characterization, Applications* (Wiley, New York, 2004).
[2]S. Minko, Polym. Rev. **46**, 397 (2006).
[3]M. A. C. Stuart, W. T. S. Huck, J. Genzer, M. Müller, C. Ober, M. Stamm, G. B. Sukhorukov, I. Szleifer, V. V. Tsukruk, M. Urban, F. Winnik, S. Zauscher, I. Luzinov, and S. Minko, Nature Mater. **9**, 101 (2010).
[4]F. Zhou and W. T. S. Huck, Phys. Chem. Chem. Phys. **8**, 3815 (2006).
[5]W. J. Brittain and S. Minko, J. Polym. Sci. A **45**, 3505 (2007).
[6]J. H. Dorsey and K. A. Dill, Chem. Rev. **89**, 331 (1989).
[7]D. Cunliffe, C. de las Heras Alarcon, V. Peters, and C. Alexander, Langmuir **19**, 288 (2003).
[8]I. Y. Galaev and B. Mattiasson, J. Chromatogr., A **662**, 27 (1994).
[9]S. Alexander, J. Phys. (France) **38**, 983 (1977).
[10]P. G. de Gennes, Macromolecules **13**, 1069 (1980).
[11]J. Ruhe, M. Ballauff, M. Biesalski, P. Dziezok, F. Grohn, D. Johannsmann, N. Houbenov, N. Hugenberg, R. Konradi, S. Minko, M. Motornov, R. R. Netz, M. Schmidt, C. Seidel, M. Stamm, T. Stephan, D. Usov, and H. N. Zhang, Adv. Polym. Sci. **165**, 79 (2004).
[12]S. T. Milner, T. A. Witten, and M. E. Cates, Macromolecules **21** 2610 (1988).
[13]E. B. Zhulina, O. V. Borisov, V. A. Pryamitsyn, and T. M. Birshtein, Macromolecules **24**, 140 (1991).
[14]G. J. Fleer, A. A. Cohen Stuart, J. M. H. M. Scheutjens, T. Cosgrove, and B. Vincent, *Polymers at Interfaces* (Chapman and Hall, London, 1993).
[15]M. A. Carignano and I. Szleifer, J. Chem. Phys **100**, 3210 (1994); **102**, 8662 (1995); Macromolecules **28**, 3197 (1995).
[16]P. Bryk and L. G. MacDowell, J. Chem. Phys. **129**, 104901 (2008).
[17]J. D. McCoy, M. A. Teixeira, and J. G. J. Curro, J. Chem. Phys. **113**, 4289 (2001).
[18]Y. Ye, J. D. McCoy, and J. G. J. Curro, J. Chem. Phys. **119**, 555 (2003).
[19]T. Jiang, Z. Li, and J.-Z. Wu, Macromolecules **40**, 334 (2007).
[20]M. Borówko, W. Rżysko, S. Sokołowski, and T. Staszewski, J. Chem. Phys. **126**, 214703 (2007).
[21]A. Milchev, S. A. Egorov, and K. Binder, J. Chem. Phys. **132**, 184905 (2010).
[22]P. Y. Lai, J. Chem. Phys. **98**, 669 (1993).
[23]G. S. Grest and M. Murat, Macromolecules **26**, 3108 (1993).
[24]J. D. Weinhold and S. K. Kumar, J. Chem. Phys. **101**, 4312 (1994).
[25]S. J. Klatte and T. L. Beck, J. Chem. Phys. **100**, 5931 (1996).
[26]G. S. Grest, J. Chem. Phys. **105**, 5532 (1996).
[27]I. Yarovsky, M. I. Aguilar, and M. T. Hearn, Anal. Chem. **68**, 1974 (1996).
[28]K. A. Lippa, L. C. Sander, and R. D. Mountain, Anal. Chem. **77**, 7862 (2005).
[29]K. Ban, Y. Saito, and K. Jinno, Anal. Sci. **21**, 397 (2005).
[30]K. Ohno, T. Sakamoto, T. Mingawa, and Y. Okabe, Macromolecules **40**, 723 (2007).
[31]J. L. Rafferty, J. I. Siepmann, and M. R. Schure, J. Chromatogr., A **1204**, 20 (2008); Anal. Chem. **80**, 6214 (2008); J. Chromatogr., A **1216**, 2320 (2009).
[32]L. G. MacDowell and M. Müller, J. Chem. Phys. **124**, 084907 (2006).
[33]Y. Kong, C. W. Manke, W. G. Madden, and A. G. Schlijper, Int. J. Thermophys. **15**, 1093 (1994).
[34]J. B. Gibson, K. Chen, and S. Chynoweth, J. Colloid Interface Sci. **206**, 464 (1998).
[35]M. G. Saphiannikova, V. A. Pryamitsyn, and T. Cosgrove, Macromolecules **31**, 6662 (1998).
[36]P. Malfreyt and D. J. Tildesley, Langmuir **16**, 4732 (2000).
[37]F. Goujon, P. Malfreyt, and D. J. Tildesley, Chem. Phys. Chem. **5**, 457 (2004); Mol. Phys. **103**, 2675 (2005).
[38]C. M. Wijmans and B. Smit, Macromolecules **35**, 7138 (2002).
[39]C. Pastorino, K. Binder, T. Keer, and M. Mueller, J. Chem. Phys. **124**, 064902 (2006).
[40]C. Pastorino, K. Binder, and M. Muller, Macromolecules **42**, 401 (2009).
[41]M. Patra and P. Linse, Nano Lett. **6**, 133 (2006).
[42]F. Goujon, P. Malfreyt, and D. J. Tildesley, J. Chem. Phys. **129**, 034902 (2008).
[43]C.-S. Li, W.-C. Wu, Y.-J. Sheng, and W.-C. Chen, J. Chem. Phys. **128**, 154908 (2008).
[44]P. Petrus, M. Lísal, and J. K. Brennan, Langmuir **26**, 3695 (2010); *ibid*. **26**, 14680 (2010).
[45]Y.-H. Xue, H. Liu, Z.-Y. Lu, and X.-Z. Liang, J. Chem. Phys. **132**, 044903 (2010).
[46]P. J. Hoogerbrugge and J. M. A. Koelman, Europhys. Lett. **19**, 155 (1992).
[47]P. Español and P. Warren, Europhys. Lett. **30**, 191 (1995).
[48]B. Smit and D. Frenkel, *Understanding Molecular Simulation*, 2nd ed. (Academic, New York, 2002).
[49]D. W. L. Tolfree, Rep. Prog. Phys. **61**, 313 (1998); F. Burmeister, C. Schläfle, B. Keilhofer, C. Bechinger, J. Boneberg, and P. Leiderer, Adv. Mater. **10**, 495 (1998); A. Kumar and G. M. Whitesides, Appl. Phys. Lett. **63**, 2002 (1993); J. L. Wilbur, A. Kumar, E. Kim, and G. M. Whitesides, Adv. Mater. **6**, 600 (1994); J. B. Knight, A. Vishwanath, J. P. Brody, and R. H. Austin, Phys. Rev. Lett. **80**, 3863 (1998).
[50]*Surface-Initiated Polymerization I and II*, Advances in Polymer Science Vol. 197/198, edited by R. Jordan (Springer, Berlin, 2006); X. Zhou, Y. Chen, B. Li, G. Lu, F. Y.C. Boey, J. Ma, and H. Zhang, Small **4**, 1324 (2008); Q. He, A. Kueller, S. Schilp, F. Leisten, H.-A. Kolb, M. Grunze, and J. Li, Small **3**, 1860 (2007); U. Schmelmer, A. Paul, A. Küller, M. Steenackers, A. Ulman, M. Grunze, A. Gölzhäuser, and R. Jordan, Small **3**, 459 (2007).
[51]A. Jayaraman, C. K. Hall, and J. Genzer, J. Chem. Phys. **123**, 124702 (2005); P. Adamczyk, P. Romiszowski, and A. Sikorski, Catal. Lett. **129**, 130 (2009); H. Chen, C. Peng, L. Sun, H. Liu, Y. Hu, and J. Jiang, Langmuir **23**, 11112 (2007); A. G. Koutsioubas and A. G. Vanakaras, Langmuir **24**, 13717 (2008); H. Chen, C. Peng, Z. Ye, H. Liu, and Y. Hu, Langmuir **23**, 2430 (2007); H. Chen, X. Chen, Z. Ye, H. Liu, and Y. Hu, Langmuir **26**, 6663 (2010).
[52]D. Petera and M. Muthukumar, J. Chem. Phys. **107**, 9640 (1997); **109**, 5101 (1998); K. Ch. Daoulas, M. Müller, M. P. Stoykovich, H. Kang, J. J. de Pablo, and P. F. Nealey, Langmuir **24**, 1284 (2008).
[53]R. D. Groot and P. B. Warren, J. Chem. Phys. **107**, 4423 (1997).
[54]J. M. Ilnytskyi and Yu. Holovatch, Condens. Matt. Phys. **10**, 539 (2007).
[55]J. M. Ilnytskyi, T. Patsahan, M. Holovko, P. E. Krouskop, and M. P. Makowski, Macromolecules **41**, 9904 (2008).
[56]D. C. Visser, H. C.J. Hoefsloot, and P. D. Iedema, J. Comput. Phys. **205**, 626 (2005).
[57]I. V. Pivkin and G. E. Karniadakis, J. Comput. Phys. **207**, 114 (2005); I. V. Pivkin and G. E. Karniadakis, J. Chem. Phys. **124** 184101 (2006); F. Jian, H. Yongmin, L. Honglai, and H. Ying, Front. Chem. Eng. China **1**, 132 (2007).
[58]J. B. Gibson, K. Zhang, K. Chen, S. Chynoweth, and C. W. Manke, Mol. Simul. **23**, 1 (1999); M. Revenga, I. Zúñiga, P. Español, and I. Pagonabarraga, Int. J. Mod. Phys. C **9**, 1319 (1998).
[59]K. E. Novik and P. V. Coveney, Phys. Rev. E **61**, 435 (2000); Y. Zhao, H. Liu, Z.-Y. Lu, and C.-C. Sun, Chin. J. Chem. Phys. **21**, 451 (2008).
[60]M. Bishop and M. J. Michele, J. Chem. Phys. **84**, 444 (l986); K. Kremer and G. S. Grest, J. Chem. Phys. **92**, 5057 (1990); G. Zimpferer, Macromol. Theory Simul. **8**, 433 (1999).